

OReole-FM: successes and challenges toward billion-parameter foundation models for high-resolution satellite imagery

Philipe Dias
Aristeidis Tsaris
ambroziodiap@ornl.gov
Oak Ridge National Laboratory
Oak Ridge, Tennessee, USA

Jordan Bowman
Abhishek Potnis
Jacob Arndt
Oak Ridge National Laboratory
Oak Ridge, Tennessee, USA

H. Lexie Yang
Dalton Lunga
lungadd@ornl.gov
Oak Ridge National Laboratory
Oak Ridge, Tennessee, USA

Abstract

While the pretraining of Foundation Models (FMs) for remote sensing (RS) imagery is on the rise, models remain restricted to a few hundred million parameters. Scaling models to billions of parameters has been shown to yield unprecedented benefits including emergent abilities, but requires data scaling and computing resources typically not available outside industry R&D labs. In this work, we pair high-performance computing resources including Frontier supercomputer, America's first exascale system, and high-resolution optical RS data to pretrain billion-scale FMs. Our study assesses performance of different pretrained variants of vision Transformers across image classification, semantic segmentation and object detection benchmarks, which highlight the importance of data scaling for effective model scaling. Moreover, we discuss construction of a novel TIU pretraining dataset, model initialization, with data and pretrained models intended for public release. By discussing technical challenges and details often lacking in the related literature, this work is intended to offer best practices to the geospatial community toward efficient training and benchmarking of larger FMs.

Keywords

Foundation Models, Remote Sensing, Earth Observation, Self-supervised learning, High-resolution satellite imagery

1 Introduction

Remote sensing (RS) imagery interpretation remains pivotal to understanding of the Earth surface, with Earth Observation (EO) applications including mapping of built environments [3], disaster management [29], and gravity mapping [54]. While deep neural networks (DNN) and computer vision have enable extraordinary progress in interpretation of imagery, most DNNs are task-specific, with limited generalization to out-of-distribution data, and rely on the onerous availability of large quantities of manually annotated data samples.

Recently, Foundation Models (FMs) have emerged as a breakthrough with potential to address limitations of neural networks in

terms of task-specificity, poor generalization to out-of-distribution data, and reliance on labeled data. FMs can be defined as large models ($> 10^8$ parameters) usually trained via self-supervised learning (SSL) on vast data volumes, and are characterized by extraordinary transfer learning capabilities on a wide range of downstream tasks.

A growing body of self-supervised studies is emerging in the remote sensing community, and Vision Transformers (ViTs) [20] are by far dominating the large scale interpretation of remote sensing imagery. Table 1 provides a summary on the state-of-the-art works pairing self-supervised learning and remote sensing data, along with model size configurations. Compared to the 100B+ parameters powering modern LLMs, current FMs for RS are only up to few hundred million parameters. LLMs such as LLAMA (65B) [42], GPT-3 (175B) [7] and PaLM (540B) [13], while ViT-based structures have been extended for up to 20B+ parameters [17]. Importantly, studies in both NLP and computer vision have shown how scaling model capacity enables highly capable and generalizable FMs, including enabling the so-called emergent abilities: i.e., capabilities that are not present in smaller-scale models but are present in large-scale models, and cannot be predicted by simply extrapolating the performance improvements on smaller-scale models. Examples include capabilities that the model is not explicitly programmed or optimized for, such as NLP models trained for predicting the next word

Table 1: A comparison of model sizes for current state-of-the-art foundation models for Earth observation.

Model	Backbone	Parameters
GASSL [4]	ResNet-50	~ 25M
SeCo [34]	ResNet-50	~ 25M
SatMAE [15]	ViT-L	~ 307M
ScaleMAE [37]	ViT-L	~ 307M
RVSA [47]	ViT/ViTAE*-B	~ 110M
RingMo [40]	Swin/ViT-B	~ 100M
Prithvi [27]	ViT-L	~ 307M
Satlas [5]	Swin-B	~ 100M
GFM [35]	Swin-B	~ 100M
USat [26]	ViT-L	~ 307M
MTP [46]	ViT-L/InternImage-XL	~ 307/335M
SkySense[23] ¹	Swin-H	~ 654M
OReole-MR/-HR	ViT-e (3B)	~ 3B

¹ SkySense includes separate encoders for high-resolution (Swin-H) and medium-resolution (ViT-L, 302M) optical imagery, SAR (ViT-L, 302M). Combined, all modules composing the model add up to 2B parameters;

This is the author's full version of the work, published in ACM SIGSPATIAL 2024 as a short paper. Not for redistribution. The definitive Version of Record was published in <https://doi.org/10.1145/3678717.3691292>. This manuscript has been authored by UT-Battelle, LLC, under contract DE-AC05-00OR22725 with the US Department of Energy (DOE). The US government retains and the publisher, by accepting the article for publication, acknowledges that the US government retains a nonexclusive, paid-up, irrevocable, worldwide license to publish or reproduce the published form of this manuscript, or allow others to do so, for US government purposes. DOE will provide public access to these results of federally sponsored research in accordance with the DOE Public Access Plan (<http://energy.gov/downloads/doe-public-access-plan>). This research used resources of the Oak Ridge Leadership Computing Facility, which is a DOE Office of Science User Facility supported under Contract DE-AC05-00OR22725.

in a sentence developing abilities to perform translation between languages or multiplying numbers [49].

However, scaling models to billions of parameters commands significant computing resources that have been typically restricted to on-premise high-performance computing (HPC) resources not available to researchers outside industry R&D labs. The ViT-22B described in [17] by Google Research was trained on 1024 TPU V4 chips, while the training of LLaMA by Meta AI on its 65B-parameter configuration was performed using 2048 NVIDIA A100 (80GB) GPUs [42]. In addition to the accessibility to such computing resources, the expertise and best practices on how to leverage them effectively to train FMs remains limited to few established organizations.

In this paper, we pretrain and evaluate billion-scale FMs for RS data analysis by leveraging the exascale Frontier Supercomputer [1]- the first exascale high performance computer. The study represents an initial step part of a broader agenda targeting best practices for training FMs, construction of pretraining datasets, benchmarking, and increasing the practical use of FMs for RS. As main contributions, we introduce:

- The OREOLE family of FMs for EO. The OREOLE-MR variant is pretrained on the MillionAID dataset of aerial RGB remote sensing images. Meanwhile, the OREOLE-HR is trained on very high-resolution BGR+NIR satellite imagery, targeting applications such as building footprint mapping [33, 53] and damage assessment [19] that are critical for, e.g., the development of LandScan’s population maps [6, 38].
- ViT-based models scaled into the billion-parameter range, discussing successes, recommended HPC practices, as well as challenges for pretraining and evaluation;
- **TIU**, a high-resolution RS imagery pretraining dataset that considers geographic, temporal, and image collection characteristics to benefit dataset diversity and representativeness;
- A transfer learning technique for initialization of a 4-band model using pretrained weights from a 3-band (RGB) model, improving pretraining speed and downstream performance;
- All models, codes, and datasets in this work are intended for public release. Once approved, together with supplementary materials they will be published to geoai.ornl.gov.

2 Related Works

Key ingredients for developing FMs. By leveraging surrogate tasks as sources of supervision, self-supervised learning (SSL) unlocks the potential of learning from unprecedentedly large unlabeled datasets for which manual labeling would be unfeasible, thus underpinning the success of FMs. Masked modeling and contrastive learning (CL) have been the two prevailing approaches for SSL of computer vision models. Generative modeling schemes such as masked language modelling were key enablers for, e.g., GPT and BERT models [18, 36]. They have been analogously explored for

computer vision in the form of masked image modeling (MIM) [24], where the model is tasked to reconstruct pixels of masked image patches based on the remaining visible image patches. Alternatively, CL schemes task models to maximize feature similarity for correlated image views constructed through augmentations [10].

To enable scaling models to billions of parameters, in addition to SSL three key ingredients have been needed: scalable architectures, large data volumes, and computational resources. Transformer-based architectures [44] have been widely used across domains, including Vision Transformers (ViT) [20] for scalable image analysis models [17, 57]. As discussed in [52], large models can easily overfit if data volumes are not scaled accordingly. Combined to the need for long pretraining, this implies the need for leveraging HPC resources for both fitting larger models in GPU memory, as well as enabling distributed data parallelism.

Foundation models in RS. Transformer-based architectures have been the predominant strategy in works discussing FMs for RS. Masked Autoencoder (MAE) has been predominant for SSL, including SatMAE [15], Ringmo [40], Prithvi [27], [25], SATLASNet [5] and most recently the billion-scale foundation model (BFM) for remote sensing images [8]. Works including SeCo [34], GASSL [4], and Skysense [23] employ Contrastive Learning (CL) instead. In contrast to natural images, RS imagery allows leveraging image acquisitions covering the same location, but from different timestamps and sensors as augmentations for CL. Both GASSL and SeCo are designed to exploit spatially aligned images and temporal information to obtain seasonal positive pairs of images at different points in time for training seasonal contrasting learning objectives. In contrast, Skysense exploits features in a multi-granularity scheme to learn representations across different modal and spatial granularities.

Model’s architecture and training regime that exploit the characteristic features intrinsic in remote sensing imagery have been introduced, including image content [47], spectra [25], multi-scale features [37], temporal characteristics [15, 27]. As summarized in Table 1, with the exception of Skysense[23] all the aforementioned works consists of models whose architectural number of parameters is less than 300-million and are trained on datasets whose corpus is no where near the internet scale volumes encountered when training LLMs. Scaling the architectural sizes of FMs has been shown to bring forth many desirable benefits including task generalization and label efficiency. For these reasons, we contrast our work by introducing a systematic study profiling billion scale models pretrained on globally diversified high resolution satellite imagery.

3 Methods

All OREOLE-MR/-HR models are “vanilla” ViTs paired with MAE pretraining. We opt for such simpler configurations to focus on assessing model scaling effects. Future work will explore leveraging unique geospatial and temporal data characteristics, such as GSD-aware positional encodings [37], contrastive learning using multiple collections over same location, and other architectural strategies such as RVSA [47].

Model Architecture Variants Table 2 summarizes the different ViT variants explored in this work. *Width* corresponds to embedding size, *depth* corresponds to number of encoding layers, while

OREole is a play of words. OR alludes to the Oak Ridge National Laboratory, where this research is conducted. We believe birds are a great metaphor for such models for Earth Observation (“eyes from above”), and found the oriole family to be a perfect fit: orioles are songbirds found in many regions throughout the world, and their colorful feathers also offer a metaphor for the multimodality intended for this family of models. We then slightly adapt the name by including ‘EO’.

heads denote the number of heads per self-attention layer. While ViT-B configurations are paired with input patches 16×16 pixels large, all other larger ViT variants are paired with 14×14 pixels patches as per [20] and related works. The study in [20] discusses how scaling all aspects (i.e., depth, width, MLP-width, and patch-size) by similar amounts is most effective, while [57] performs extensive simulations to define ViT variants of different sizes. We follow these empirical guides and [17] (ViT-22B) to increase the number of encoder layers and heads by gradually scaling the embedding size from 768 to 2816. The decoder pretraining architecture follows the original MAE work [24].

Table 2: ViT variants for OReOLE models

Model	Width	Depth	MLP	Heads	Parameters
ViT-B	768	12	3072	12	87M
ViT-H	1280	32	5120	16	635M
ViT-G (1B)	1536	32	6144	16	914M
ViT-e (3B)	2816	32	11264	32	3067M

Scalability strategies As part of this research, in [43] we discuss studies using the Frontier supercomputer on model sharding and data parallelism. Main observations include: i) FSDP-enabled implementations provide significant throughput gains when compared to PyTorch’s DDP; ii) communication overheads rather than file I/O become the main bottleneck for such MAE-type of workloads. We refer the interested reader to [43] for further discussions on model sharding strategies and weak scaling studies. In the sections that follow, we adopt such a FSDP-enabled implementation for model pretraining.

Pretraining configuration Table 3 summarizes the pretraining datasets and duration for OReOLE models and related works, which highly vary in pretraining durations (up to 1600M+ iterations). We pretrain OReOLE models for $\approx 200M$ iterations, as a trade-off between long enough pretraining to enable generalizable models while avoiding indiscriminate usage of computing resources. Details on code-bases used for pretraining are available in the Appendix.

3.1 Pretraining datasets

Even though SSL removes the needs for data annotation, the acquisition of pretraining samples ought to be carefully designed. In the context of geospatial data, key characteristics to be considered during dataset curation include geographic diversity, richness, and scalability, to foment the learning of generic representations.

Examples of high-resolution RS datasets attempting to capture these characteristics include the MillionAID and the functional map of the world (fMoW). The fMoW dataset [14] used by [15, 37] contains 500k+ optical patches collected from multiple sensors. In contrast, the MillionAID [32] used by [8, 47] contains 1M+ RS scenes from a variety sensors and ground sample distances (GSD=0.5-150m/px). RingMo instead [40] exploits a not publicly-available dataset containing 2M+ images for 419M iterations.

Given the compute intense demands for pretraining FMs and the lack of standardized datasets, early studies have sought to pretrain on a single benchmark dataset[4, 8, 37, 47], while other studies

merge multiple data sources to increase the volume and diversity of samples[40]. A growing body of work[5, 23, 27, 34, 39] is curating multimodal datasets sampled from large archives of remote sensing imagery including national agricultural imagery program (NAIP), Sentinel-1/-2, Harmonized Landsat Sentinel-2 (HLS), or WorldView-2/-3. We introduce two additional datasets in this paper, including the novel TIU.

Table 3: Pretraining datasets and configurations.

Dataset	Bands	GSD [m/px]	Volume [~TB]	Iterations		
				RVSA	BFM	OReole
MillionAID	RGB	0.5-153	0.14	1601.4M	400.3M	200.2M
ORB	BGR+NIR	≈ 0.47	0.70	-	-	202.1M
TIU	BGR+NIR	0.3-0.8	1.30	-	-	202.1M

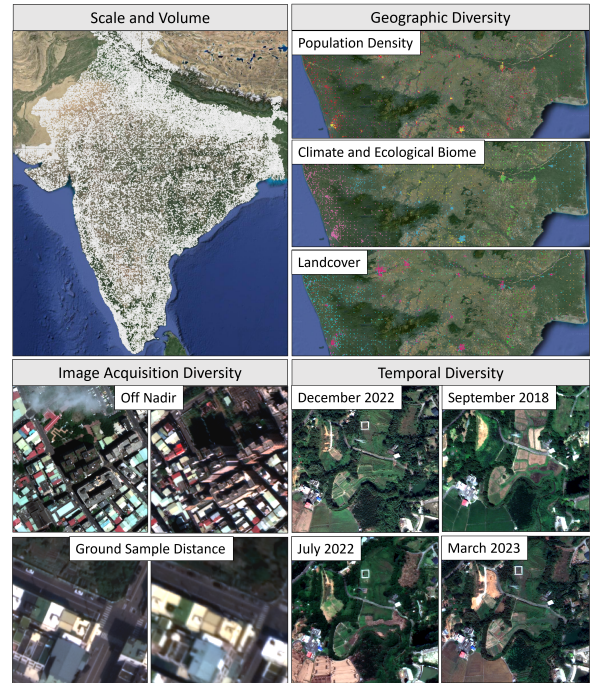


Figure 1: Illustration of characteristics of the TIU dataset.

ORBITaL-Net. ORBITaL-Net [41] (ORB for shortness) is a semantic segmentation dataset for building footprint extraction (BFE) from high-resolution BGR+NIR imagery. The dataset includes $\approx 126k$ samples collected across diverse geographic regions including North America, Asia, Africa, South America, and the Middle East. Samples in this dataset consist of four channels (blue, green, red, near-infrared), were collected by the GeoEye-1, QuickBird-2, WorldView-2, and WorldView-3 sensors, have average ground sample distance of 0.47m/px, and include binary masks to support the finetuning of FMs on a downstream building segmentation task.

TIU. TIU is an unlabeled dataset we constructed using the sampling strategy from [2]. It promotes diversity in: i) *geography* by

referencing existing geographic information including population density, land cover, climate zones, and ecological biomes during sampling; ii) *temporality* by including multiple views of the same location across different meteorological seasons (e.g. spring, summer, fall, winter) and years; iii) *image acquisition* by including views from different sensors and viewing geometries. TIU consists of $\approx 170k$ BGR+NIR images from GeoEye-1, WorldView-2/3 sensors, $1024 \times 1024px$ large at $GSD = 0.3-0.8m/px$, sampled from $\approx 80k$ locations across Taiwan, India, and Ukraine, with $\approx 60\%$ of the locations with non-zero 24-hour population estimates. It contains up to four temporal views per location, each from a different meteorological season between years 2015 and 2023. Figure 1 illustrates characteristics of the dataset.

4 OREOLE-MR Experiments

We perform fine-tuning (FT) and linear probing (LP) experiments for comparison with existing baselines. Following the community trend, we consider image classification, object detection, and semantic segmentation downstream tasks. There is, however, a wide variability on the datasets used for performance benchmarking. We summarize in Table 4 the datasets commonly used to benchmark models pretrained on medium-to-high resolution imagery. Guided by this review, we selected the following datasets to compose the evaluation scenarios for OREOLE-MR variants: i) *image classification*: UCM [55], AID [50], and NWPU[11]; ii) *object detection*: DIOR [30] and DIOR-R [12]; iii) *semantic segmentation*: Potsdam and LoveDA [48]. Details on the composition of these datasets and finetuning configurations are available in the Appendix. Results are summarized in Table 5, with main takeaways discussed below.

Table 4: Summary of datasets used in related works for evaluation of downstream capabilities of pretrained models. In bold: the datasets selected for evaluation of OREOLE-MR.

	Evaluation datasets		
	<i>Image Classification</i>	<i>Object Detection</i>	<i>Semantic Segmentation</i>
RVSA	UCM, AID, NWPU	DIOR-R, DOTA-V1.0	Potsdam, iSAID, LoveDA
RingMo	UCM, AID, NWPU	DIOR, FAIR-1M	Potsdam, iSAID
MTP	EuroSAT, NWPU	DIOR/-R, FAIR1M, DOTA V1.0/V2.0	SpaceNetv1, LoveDA
BFM	-	DIOR-R, DOTA-V2.0	Potsdam, LoveDA
QUETZAL-MR	UCM, AID, NWPU	DIOR, DIOR-R	Potsdam, LoveDA

Hyperparameters used by related works are often suboptimal, and may vary with model sizes and downstream tasks. Similar to [47], we opt for linear probing for image classification experiments, since these datasets have nearly saturated for FT. Critically, experiments using ViT-B pretrained checkpoints from [47] show that for the configurations reported in [47], increasing the

Table 5: Results across: image classification (top); object detection and semantic segmentation (bottom).

	Model	Pretrain epochs	NWPU (TR=10%)	UCM (TR=50%)		AID (TR=20%)	
				LP	FT	LP	FT
ViT-B [47]	LR=0.1	1600	60.19	40.15	-	60.17	-
	LR=10	1600	87.20	98.58	-	93.84	-
OREOLE-MR	ViT-B	200	86.19	97.35	99.05	93.70	94.73
	ViT-H	200	89.73	98.39	99.24	94.76	96.15
	ViT-G (1B)	200	79.54	94.22	99.24	89.38	96.71
	ViT-e (3B)	200	89.27	98.30	-	95.53	-

Method	Backbone	Obj. detection		Segmentation	
		DIOR	DIOR-R [mAP ₅₀]	Potsdam [mF1 %]	LoveDA [mIoU %]
GASSL	ResNet-50	67.40	65.65	91.27	48.76
MAE [47]	ViT-B	-	66.65	90.32	51.09
RVSA [46]	ViT-B+RVSA	75.80	70.85	90.77	51.95
MTP [46]	ViT-B+RVSA	79.40	-	-	52.39
RVSA [46]	ViT-L+RVSA	78.30	-	-	53.72
MTP [46]	ViT-L+RVSA	81.10	-	-	54.17
SatMAE	ViT-L	70.89	65.66	90.63	-
GFM	Swin-B	72.84	67.67	91.85	-
ScaleMAE	Swin-B	73.81	66.47	91.54	-
RingMo(ISSP)	Swin-B	73.50	-	91.27	-
RingMo [40]	Swin-B	75.90	-	91.74	-
BFM [8]	ViT-B	-	68.52	-	-
BFM [8]	ViT-L (605M)	-	72.11	91.75	52.38
BFM [8]	ViT-H (1.36B)	-	73.15	92.02	53.20
BFM [8]	ViT-G (2.42B)	-	73.62	92.12	54.40
SkySense	Swin-L	76.74	-	92.86	-
SkySense	Swin-H	78.73	-	93.99	-
MAE ^o	ViT-B	-	-	91.82	52.97
OREOLE-MR	ViT-B	75.50	68.58	92.01	52.44
OREOLE-MR	ViT-H	N/A ²	N/A ²	92.18	53.83
OREOLE-MR	ViT-G (1B)	77.40	71.31	92.20	54.00

¹ Since GASSL, SatMAE, ScaleMAE, and GFM did not provide evaluation on DIOR(-R) and Potsdam in their original papers, we rely on results provided in [23, 46, 47].

² Results are not available due to convergence issues.

base learning rate (LR) from 0.1 up to 10 highly increases LP accuracy.

Similarly, for object detection increasing the base LR of OREOLE-MR by $3\times$ improved ViT-G (1B) performance by nearly $+2.0\%$ in DIOR-R. Still, neither the configurations adopted for ViT-B nor ViT-G (1B) avoided loss divergence for ViT-H and ViT-e(3B) models. We conjecture two reasons: i) the object detection head is more complex, including RPN and RoI heads each with different regression losses (in contrast, e.g., to cross-entropy based optimization of UperNets for semantic segmentation); ii) related studies [31] highlight the need for different learning decay policies for different model sizes.

For semantic segmentation, [8, 47] employ 160k iterations ($BS=8$) for both datasets, while [40] and [23] use 80k. These setups equate to 1.28M and 0.64M iterations at $BS=1$. For higher efficiency, we conducted experiments using distributed computing (effective $BS=256$)

for only 0.42M (Potsdam) and 0.346M (LoveDA) iterations at $BS = 1$. Our ViT-B surpasses [47] by $> +1\%$ in both datasets, despite both pretrained and finetuned for $2x$ fewer iterations. Moreover, the MAE[◇] resulting from finetuning RVSA ViT-B checkpoints [47] with our hyperparameters significantly surpasses results in [47].

These observations indicate that configurations reported in the literature have been often suboptimal, and underscore an open challenge on how to establish standardized benchmarking practices.

Model scaling is beneficial, but with diminished gains without data scaling. For LP image classification with OREOLE-MR variants ($LR = 10$), scaling from ViT-B(87M) to ViT-H (635M) yields gains, but they are diminished when scaling further into ViT-e (3B), with improvements only observed for AID. For object detection experiments, despite using a vanilla oriented-faster RCNN, for both DIOR and DIOR-R our ViT-B performs comparably to BFM, whose detection heads employ advanced ROI transformers. In general, the scaling benefits in model sizes (ViT-B to ViT-G) is clear for both datasets, and comparisons with BFE suggest the usage of ROI transformer provides further benefits when scaling models.

For semantic segmentation, benefits of model scaling are particularly evident for LoveDA, but gains are diminished when scaling from ViT-H (635M) to ViT-G (1B). Considering discussions in the computer vision literature [52] and OREOLE-HR results discussed in the next section, we conjecture 1B+ models require further data scaling. Contrasting datasets, the MillionAID used for OREOLE-MR is $10\times$ smaller than the TIU dataset that successfully enabled OREOLE-HR’s ViT-H. Pretraining duration is another potential factor: while OREOLE-MR ViT-B performs on par with BFM’s, it is pretrained for $0.5\times$ iterations, and larger models have been shown to benefit more from data scaling when pretraining is longer [52]. OREOLE-MR’s ViT-H (635M) variant also performs comparably to the BFM’s 1B+ models [8], representing a stronger baseline to improve upon.

MAE-learned features may have limited linear separability Surprisingly, ViT-G (1B) underperforms smaller models across all LP experiments. Since the same model however outperforms smaller configurations in other tasks, we conjectured the features learned through MAE pretraining have limited linear separability. To confirm, we ran FT image classification experiments that show instead saturation for UCM, and diminished yet positive gains for AID. This is consistent with reports in the literature of MAE often underperforming, e.g., CL in LP, since pixel-reconstruction pretraining foments focus on high-frequency details, rather than semantics.

Many works lack reproducibility details for downstream evaluation Experiments using smaller portions of labeled data (available in supplementary material) highlight a lack of reproducibility details on related works. They often report maintaining the same FT configuration when varying data percentages, which is unclear when training schedules are reported in terms of epochs. We opted for maintaining the same number of training iterations for all data budgets, since the goal is to assess model’s sample efficiency, not sensitivity to duration. Our results show model scaling benefits for as low as $> 10\%$ training images of DIOR-R are used, and 1% for segmentation experiments. Notably, our ViT-B at lower sample

budgets significantly surpass numbers in [8], which we conjecture is due to our FT maintaining original training duration.

5 OREOLE-HR experiments

We leverage the ORB dataset for OREOLE-HR experiments. A separate random subset of 4,836 tiles is used for validation, and two FT configurations were considered: $TR = 100\%$, with 55.71k labeled training tiles and FT for 100 epochs (5.57M iterations); $TR = 10\%$, using 5,571 (10%) randomly sampled tiles for FT (100 epochs = 557.1k iterations). Results are summarized in Table 6 and discussed below.

Table 6: OREOLE-HR results on ORBiTal-Net dataset.

Method	Pretrain dataset	BFE - mF1[%]			
		$TR = 100\%$		$TR = 10\%$	
		ViT-B	ViT-H	ViT-B	ViT-H
No pretrain	-	91.80	-	74.68	-
MAE	ORB	91.79	91.31	89.57	88.59
MAE	TIU	92.05	92.54	89.85	91.13
O-MR [†] MAE	TIU	92.15	-	90.17	-
MAE	TIU+ORB	91.94	92.84	90.07	91.70
MAE (224 px^2)	TIU+ORB	-	-	-	90.38

[†] initialized with MillionAID pretrained OREOLE-MR weights inflated to 4-bands.

Pretraining on ORB dataset vs no pretrain (ViT-B) While MAE pretraining on the same ORB dataset used for finetuning does not improve F1 in the $TR = 100\%$ configuration, results in the $TR = 10\%$ regime does reveal a significant benefit of pretraining in improving the time-to-solution (i.e. consumes less computing resources).

Model scaling requires data scaling, and larger models benefit more from data scaling ViT-H models pretrained on the ORB dataset are worse than ViT-B for both TR configurations. In contrast, pretraining with the larger TIU dataset enables ViT-H model to significantly outperform ViT-B in both TRs configurations. Compared to ViT-B counterparts ($-0.11/+0.22\%$), the higher capacity ViT-H also benefits more from pretraining on the larger TIU+ORB dataset as compared to TIU only, with F1 for $TR = 10\%$ similar to the ones obtained by ViT-B in $TR = 100\%$ configuration.

Initialization using inflated OREOLE-MR weights. Aiming speed-ups in training convergence and improved feature extraction, prior to MAE pretraining our O-MR+MAE configuration initializes a ViT-B with RGB OREOLE-MR pretrained weights, inflated with extra 4th-band randomly initialized weights. Results corroborate that the model’s intrinsic exposure to MillionAID’s images provide indirect data scaling benefits, with F1 rates boosted for both TR settings in comparison to TIU-only pretraining.

Pretraining using larger image sizes While pretraining a ViT-H using 224 2px instead of 512 2px patches reduces GPU usage in $> 4\times$, our experiments have shown a -1.32% F1 drop for $TR = 10\%$ finetuning. This indicates that pretraining with larger patches can significantly benefit fine-grained tasks if computing can be afforded.

6 Conclusion

We introduced OREOLE, a family of FMs for RS image interpretation. Experiments with OREOLE-MR highlight model scaling benefits across downstream tasks, but with a pattern of diminished gains. Paired with takeaways from OREOLE-HR experiments, it highlights the importance of pairing model and data scaling, confirming for RS data a behavior observed in the broader computer vision [52].

Furthermore, we share a rare discussion on challenges related to downstream task optimization and setting up evaluation protocols. Many works lack reproducibility details such as the number of training iterations as dataset sizes vary. Moreover, we show how hyperparameters co-opted from related works can be largely sub-optimal, and how parameters are sensitive to model size and tasks. This is a challenge for benchmarking, as exhaustive hyperparameter tuning is computationally expensive and contradictory to the intended benefits of FMs. We argue in favor of benchmarks with fixed-budget hyperparameter search, as suggested in [28].

Building on these conclusions and our work [43], we aim to scale models beyond 3B parameters with expanded pretraining datasets, conduct few-shot evaluations to explore potential emergent abilities and implement geospatial-aware methods and integrate multiple data modalities to improve using FMs for Earth understanding.

References

- [1] [n. d.]. The Frontier supercomputer. <https://www.olcf.ornl.gov/frontier/>.
- [2] Jacob Arndt, Philippe Dias, Abhishek Potnis, and Dalton Lunga. 2024. Towards Diverse and Representative Global Pretraining Datasets for Remote Sensing Foundation Models. In *IEEE IGARSS*. 2723–2728.
- [3] Jacob Arndt and Dalton Lunga. 2021. Large-Scale Classification of Urban Structural Units From Remote Sensing Imagery. *IEEE Journal of Selected Topics in Applied Earth Observations and Remote Sensing* 14 (2021), 2634–2648. <https://doi.org/10.1109/JSTARS.2021.3052961>
- [4] Kumar Ayush, Burak Uzket, Chenlin Meng, Kumar Tanmay, Marshall Burke, David Lobell, and Stefano Ermon. 2021. Geography-aware self-supervised learning. In *IEEE/CVF ICCV*. 10181–10190.
- [5] Favyen Bastani, Piper Wolters, Ritwik Gupta, Joe Ferdinando, and Aniruddha Kembhavi. 2022. SatlasPretrain: A Large-Scale Dataset for Remote Sensing Image Understanding. *IEEE/CVF ICCV* (2022), 16726–16736. <https://api.semanticscholar.org/CorpusID:258947021>
- [6] Budhendra Bhaduri, Edward Bright, Phillip Coleman, and Marie L Urban. 2007. LandScan USA: a high-resolution geospatial and temporal modeling approach for population distribution and dynamics. *GeoJournal* 69 (2007), 103–117.
- [7] Tom Brown, Benjamin Mann, Nick Ryder, Melanie Subbiah, Jared D Kaplan, Prafulla Dhariwal, Arvind Neelakantan, Pranav Shyam, Girish Sastry, Amanda Askell, et al. 2020. Language models are few-shot learners. *Advances in neural information processing systems* 33 (2020), 1877–1901.
- [8] Keumgang Cha, Junghoon Seo, and Taekyung Lee. 2023. A billion-scale foundation model for remote sensing images. *arXiv:2304.05215* (2023).
- [9] Kai Chen, Jiaqi Wang, Jiangmiao Pang, Yuhang Cao, Yu Xiong, Xiaoxiao Li, Shuyang Sun, Wansen Feng, Ziwei Liu, Jiarui Xu, Zheng Zhang, Dazhi Cheng, Chenchen Zhu, Tianheng Cheng, Qijie Zhao, Buyu Li, Xin Lu, Rui Zhu, Yue Wu, Jifeng Dai, Jingdong Wang, Jianping Shi, Wanli Ouyang, Chen Change Loy, and Dahua Lin. 2019. MMDetection: Open MMLab Detection Toolbox and Benchmark. *arXiv:1906.07155* (2019).
- [10] Ting Chen, Simon Kornblith, Mohammad Norouzi, and Geoffrey Hinton. 2020. A simple framework for contrastive learning of visual representations. In *International conference on machine learning*. PMLR, 1597–1607.
- [11] Gong Cheng, Junwei Han, and Xiaoqiang Lu. 2017. Remote Sensing Image Scene Classification: Benchmark and State of the Art. *IEEE* 105, 10 (2017), 1865–1883.
- [12] Gong Cheng, Jiabao Wang, Ke Li, Xingxing Xie, Chunbo Lang, Yanqing Yao, and Junwei Han. 2022. Anchor-Free Oriented Proposal Generator for Object Detection. *IEEE Trans. on Geoscience and Remote Sensing* 60 (2022), 1–11.
- [13] Aakanksha Chowdhery, Sharan Narang, Jacob Devlin, Maarten Bosma, Gaurav Mishra, Adam Roberts, Paul Barham, Hyung Won Chung, Charles Sutton, Sebastian Gehrmann, et al. 2023. Palm: Scaling language modeling with pathways. *Journal of Machine Learning Research* 24, 240 (2023), 1–113.
- [14] Gordon Christie, Neil Fendley, James Wilson, and Ryan Mukherjee. 2018. Functional map of the world. In *IEEE CVPR*. 6172–6180.
- [15] Yezhen Cong, Samar Khanna, Chenlin Meng, Patrick Liu, Erik Rozi, et al. 2022. Satmae: Pre-training transformers for temporal and multi-spectral satellite imagery. *Advances in Neural Information Processing Systems* 35 (2022), 197–211.
- [16] MMLab Contributors. 2023. OpenMMLab’s Pre-training Toolbox and Benchmark. <https://github.com/open-mmlab/mmlabpretrain>.
- [17] Mostafa Dehghani, Josip Djolonga, Basil Mustafa, Piotr Padlewski, Jonathan Heek, Justin Gilmer, Andreas Peter Steiner, Mathilde Caron, Robert Geirhos, Ibrahim Alabdulmohsin, et al. 2023. Scaling vision transformers to 22 billion parameters. In *International Conference on Machine Learning*. PMLR, 7480–7512.
- [18] Jacob Devlin, Ming-Wei Chang, Kenton Lee, and Kristina Toutanova. 2018. Bert: Pre-training of deep bidirectional transformers for language understanding. *arXiv:1810.04805* (2018).
- [19] Philippe Dias, Jacob Arndt, Marie Urban, and Dalton Lunga. 2024. Conditional Experts for Improved Building Damage Assessment Across Satellite Imagery View Angles. In *IGARSS 2024 - 2024 IEEE International Geoscience and Remote Sensing Symposium*. 1741–1745. <https://doi.org/10.1109/IGARSS53475.2024.10640461>
- [20] Alexey Dosovitskiy, Lucas Beyer, Alexander Kolesnikov, Dirk Weissenborn, Xi-aohua Zhai, Thomas Unterthiner, Mostafa Dehghani, Matthias Minderer, Georg Heigold, Sylvain Gelly, et al. 2020. An Image is Worth 16x16 Words: Transformers for Image Recognition at Scale. In *International Conference on Learning Representations*.
- [21] GDAL/OGR contributors. 2024. *GDAL/OGR Geospatial Data Abstraction software Library*. Open Source Geospatial Foundation. <https://doi.org/10.5281/zenodo.5884351>
- [22] Ross Girshick. 2015. Fast R-CNN. In *2015 IEEE International Conference on Computer Vision (ICCV)*. 1440–1448. <https://doi.org/10.1109/ICCV.2015.169>
- [23] Xin Guo, Jiangwei Lao, Bo Dang, Yingying Zhang, Lei Yu, et al. 2023. Sky-Sense: A Multi-Modal Remote Sensing Foundation Model Towards Universal Interpretation for Earth Observation Imagery. *ArXiv abs/2312.10115* (2023).
- [24] Kaiming He, Xinlei Chen, Saining Xie, Yanghao Li, Piotr Dollár, and Ross Girshick. 2022. Masked autoencoders are scalable vision learners. In *IEEE/CVF CVPR*. 16000–16009.
- [25] Danfeng Hong, Bing Zhang, Xuyang Li, Yuxuan Li, Chenyu Li, Jing Yao, Naoto Yokoya, Hao Li, Pedram Ghamisi, Xiuping Jia, Antonio J. Plaza, Paolo Gamba, Jón Atli Benediktsson, and Jocelyn Chanussot. 2023. SpectralGPT: Spectral Remote Sensing Foundation Model. *IEEE Trans. on pattern analysis and machine intelligence* PP (2023). <https://api.semanticscholar.org/CorpusID:267628000>
- [26] Jeremy Irvin, Lucas Tao, Joanne Zhou, Yuntao Ma, Langston Nashold, Benjamin Liu, and Andrew Y Ng. 2023. USat: A unified self-supervised encoder for multi-sensor satellite imagery. *arXiv preprint arXiv:2312.02199* (2023).
- [27] Johannes Jakubik, Sujit Roy, C. E. Phillips, Paolo Fraccaro, Denys Godwin, Bianca Zadrozny, Daniela Szwarzman, Carlos Gomes, Gabby Nyirjesy, Blair Edwards, Daiki Kimura, Naomi Simumba, Linsong Chu, S. Karthik Mukkavilli, Devyani Lambhate, Kamal Das, Ranjini Bangalore, Dario Oliveira, Michal Muszynski, Kumar Ankur, Muthukumar Ramasubramanian, Iksha Gurung, Sam Khalilagi, Hanxi, Li, Michael Cecil, Maryam Ahmadi, Fatemeh Kordi, Hamed Alemohammad, Manil Maskey, Raghu Ganti, Kommy Weldemariam, and Rahul Ramachandran. 2023. Foundation Models for Generalist Geospatial Artificial Intelligence. *arXiv:2310.18660* [cs.CV]
- [28] Alexandre Lacoste, Nils Lehmann, Pau Rodriguez, Evan Sherwin, Hannah Kerner, et al. 2024. Geo-bench: Toward foundation models for earth monitoring. *Advances in Neural Information Processing Systems* 36 (2024).
- [29] Melanie Laverdiere, Lexie Yang, Mark Tuttle, and Chris Vaughan. 2020. Rapid Structure Detection in Support of Disaster Response: A Case Study of the 2018 Kilauea Volcano Eruption. In *IGARSS 2020 - 2020 IEEE International Geoscience and Remote Sensing Symposium*. 6826–6829. <https://doi.org/10.1109/IGARSS39084.2020.9324160>
- [30] Ke Li, Gang Wan, Gong Cheng, Liqiu Meng, and Junwei Han. 2020. Object detection in optical remote sensing images: A survey and a new benchmark. *ISPRS Journal of Photogrammetry and Remote Sensing* 159 (2020), 296–307.
- [31] Yanghao Li, Hanzi Mao, Ross Girshick, and Kaiming He. 2022. Exploring plain vision transformer backbones for object detection. In *ECCV*. 280–296.
- [32] Yang Long, Gui-Song Xia, Shengyang Li, Wen Yang, Michael Ying Yang, Xiao Xi-ang Zhu, Liangpei Zhang, and Deren Li. 2021. On creating benchmark dataset for aerial image interpretation: Reviews, guidances, and million-aid. *IEEE Journal of selected topics in applied earth observations and remote sensing* 14, 4205–4230.
- [33] Dalton Lunga, Jacob Arndt, Jonathan Gerrard, and Robert Stewart. 2021. ReSFlow: A Remote Sensing Imagery Data-Flow for Improved Model Generalization. *IEEE Journal of Selected Topics in Applied Earth Observations and Remote Sensing* 14 (2021), 10468–10483. <https://doi.org/10.1109/JSTARS.2021.3119001>
- [34] Oscar Mañas, Alexandre Lacoste, Xavier Giró-i Nieto, David Vazquez, and Pau Rodriguez. 2021. Seasonal Contrast: Unsupervised Pre-Training From Uncurated Remote Sensing Data. In *IEEE/CVF ICCV*. 9414–9423.
- [35] Matias Mendieta, Boran Han, Xingjian Shi, Yi Zhu, and Chen Chen. 2023. Towards geospatial foundation models via continual pretraining. In *IEEE/CVF ICCV*. 16806–16816.
- [36] Alec Radford, Karthik Narasimhan, Tim Salimans, Ilya Sutskever, et al. [n. d.]. Improving language understanding by generative pre-training. ([n. d.]).

- [37] Colorado J Reed, Ritwik Gupta, Shufan Li, Sarah Brockman, Christopher Funk, et al. 2023. Scale-mae: A scale-aware masked autoencoder for multiscale geospatial representation learning. In *IEEE/CVF ICCV*. 4088–4099.
- [38] Kelly Sims, Andrew Reith, Elizabeth Bright, Jon Kaufman, Jordan Pyle, Julie Epting, Juan Gonzales, David Adams, Emily Powell, Matthew Urban, and Adam Rose. 2023. LandScan Global 2022. <https://doi.org/10.48690/1529167>.
- [39] Gencer Sumbul, Arne De Wall, Tristan Kreuziger, Filipe Marcelino, Hugo Costa, Pedro Benevides, Mario Caetano, Begüm Demir, and Volker Markl. 2021. BigEarthNet-MM: A Large-Scale, Multimodal, Multilabel Benchmark Archive for Remote Sensing Image Classification and Retrieval [Software and Data Sets]. *IEEE Geoscience and Remote Sensing Magazine* 9, 3 (2021), 174–180.
- [40] Xian Sun, Peijin Wang, Wanxuan Lu, Zicong Zhu, Xiaonan Lu, Qibin He, Junxi Li, Xuee Rong, Zhujun Yang, et al. 2022. Ringmo: A remote sensing foundation model with masked image modeling. *IEEE Trans. Geosci. Remote Sens.*, (2022).
- [41] Benjamin Swan, Joe Pyle, Darrell Roddy, Amy Rose, Lexie H. Yang, and Melanie Laverdiere. 2024. ORBITaL-Net Training Library for Building Extraction. *Figshare+ Dataset* (2024). <https://doi.org/10.25452/figshare.plus.25282225.v1>
- [42] Hugo Touvron, Thibaut Lavril, Gautier Izacard, Xavier Martinet, Marie-Anne Lachaux, Timothée Lacroix, Baptiste Rozière, Naman Goyal, Eric Hambro, Faisal Azhar, et al. 2023. Llama: Open and efficient foundation language models. *arXiv:2302.13971* (2023).
- [43] Aristeidis Tsaris, Philippe Dias, Abhishek Potnis, Junqi Yin, Feiyi Wang, and Dalton Lunga. 2024. Pretraining Billion-Scale Geospatial Foundational Models on Frontier. In *IEEE IPDPS Workshops*. 1036–1046.
- [44] Ashish Vaswani, Noam Shazeer, Niki Parmar, Jakob Uszkoreit, Llion Jones, Aidan N Gomez, Łukasz Kaiser, and Illia Polosukhin. 2017. Attention is all you need. *Advances in neural information processing systems* 30 (2017).
- [45] Di Wang, Jing Zhang, Bo Du, Gui-Song Xia, and Dacheng Tao. 2022. An empirical study of remote sensing pretraining. *IEEE Trans. on Geoscience and Remote Sensing* (2022).
- [46] Di Wang, Jing Zhang, Minqiang Xu, Lin Liu, Dongsheng Wang, Erzhang Gao, Chengxi Han, et al. 2024. MTP: Advancing Remote Sensing Foundation Model via Multi-Task Pretraining. *arXiv:2403.13430* (2024).
- [47] Di Wang, Qiming Zhang, Yufei Xu, Jing Zhang, Bo Du, Dacheng Tao, and Liangpei Zhang. 2022. Advancing plain vision transformer toward remote sensing foundation model. *IEEE Trans. on Geoscience and Remote Sensing* 61 (2022), 1–15.
- [48] Junjue Wang, Zhuo Zheng, Ailong Ma, Xiaoyan Lu, and Yanfei Zhong. 2021. LoveDA: A Remote Sensing Land-Cover Dataset for Domain Adaptive Semantic Segmentation. In *Neural Information Processing Systems Datasets and Benchmarks*.
- [49] Jason Wei, Yi Tay, Rishi Bommasani, Colin Raffel, Barret Zoph, Sebastian Borgeaud, Dani Yogatama, Maarten Bosma, Denny Zhou, Donald Metzler, et al. 2022. Emergent abilities of large language models. *arXiv:2206.07682* (2022).
- [50] Gui-Song Xia, Jingwen Hu, Fan Hu, Baoguang Shi, Xiang Bai, et al. 2017. AID: A Benchmark Data Set for Performance Evaluation of Aerial Scene Classification. *IEEE Trans. on Geoscience and Remote Sensing* 55, 7, 3965–3981.
- [51] Tete Xiao, Yingcheng Liu, Bolei Zhou, Yuning Jiang, and Jian Sun. 2018. Unified perceptual parsing for scene understanding. In *European conference on computer vision (ECCV)*. 418–434.
- [52] Zhenda Xie, Zheng Zhang, Yue Cao, Yutong Lin, Yixuan Wei, et al. 2023. On data scaling in masked image modeling. In *IEEE/CVF CVPR*. 10365–10374.
- [53] Hsiuhan Lexie Yang, Jiangye Yuan, Dalton Lunga, Melanie Laverdiere, Amy Rose, and Budhendra Bhaduri. 2018. Building extraction at scale using convolutional neural network: Mapping of the united states. *IEEE Journal of Selected Topics in Applied Earth Observations and Remote Sensing* 11, 8 (2018), 2600–2614.
- [54] Lexie Yang, Dalton Lunga, Dawn King, Jacob Arndt, Jordan Bowman, and Robert Stewart. 2021. Exploring Spatially Distributed Deep Learning Models for Global Gravitational Mapping. In *AGU Fall Meeting Abstracts*, Vol. 2021. Article EP12C-05, EP12C-05 pages.
- [55] Yi Yang and Shawn Newsam. 2010. Bag-of-visual-words and spatial extensions for land-use classification. In *ACM SIGSPATIAL Workshop on Advances in GIS*.
- [56] Yang You, Igor Gitman, and Boris Ginsburg. 2017. Large Batch Training of Convolutional Networks. *arXiv:1708.03888* [cs.CV]
- [57] Xiaohua Zhai, Alexander Kolesnikov, Neil Houlsby, and Lucas Beyer. 2022. Scaling vision transformers. In *IEEE/CVF CVPR*. 12104–12113.
- [58] Yanli Zhao, Andrew Gu, Rohan Varma, Liang Luo, Chien-Chin Huang, Min Xu, Less Wright, Hamid Shojanazeri, Myle Ott, Sam Shleifer, Alban Desmaison, Can Balioglu, Pritam Damania, Bernard Nguyen, Geeta Chauhan, Yuchen Hao, Ajit Mathews, and Shen Li. 2023. PyTorch FSDP: Experiences on Scaling Fully Sharded Data Parallel. *arXiv:2304.11277* [cs.DC]
- [59] Yue Zhou, Xue Yang, Gefan Zhang, Jiabao Wang, Yanyi Liu, Liping Hou, Xue Jiang, Xingzhao Liu, Junchi Yan, Chengqi Lyu, Wenwei Zhang, and Kai Chen. 2022. MMRotate: A Rotated Object Detection Benchmark using PyTorch. In *30th ACM International Conference on Multimedia*.

7 Appendix

7.1 Pretraining implementation details

Development of OREOLE-MR and OREOLE-HR models took place concomitantly. OREOLE-HR models were pretrained using the *mmpretrain* codebase [16], an open source pre-training toolbox based on PyTorch adapted using the *gdal* library [21] for ingestion of the BGR+NIR images in TIF-file format composing our *TIU* and *ORB* datasets. We opted for the *mmpretrain* for two main reasons. First, it contains implementations of a wide variety of model backbones and self-supervised learning strategies, offering flexibility for experimentation with other types of configurations in the long term. Moreover, it is part of the broader collection of repositories by OpenMMLab (e.g., *mmsegmentation*, *mmdetection* and *mmrotate*), thus potentially facilitating integration with configurations for downstream tasks.

OREOLE-HR models were all trained with an effective batch size of 4096 samples, distributed across GPUs composing nodes of the Frontier Supercomputer [1]. Each Frontier node contains 4× AMD Instinct MI250X GPU accelerators, with each MI250X comprising of 2× Graphics Compute Dies (GCDs). Since the system identifies each GCD independently, from the application perspective it can be considered that each node has a total of 8 GPUs, each with 64 GB of high-bandwidth memory. For simplicity we use the term GPU when referring to a GCD. ViT-H model variants were trained using 16 Frontier nodes (128 GPUs), while ViT-B variants were trained with 8 nodes (64 GPUs).

Meanwhile, OREOLE-MR models were pretrained using a codebase based on the original MAE work [24]. Specifically, we leverage the codebase and insights discussed in our recent work [43], which augments the original MAE codebase to enable the support for PyTorch’s native Fully Sharded Data Parallel (FSDP) strategy [58]. Our studies detailed in [43] revealed a higher image throughput and hence time to solution for MAE pretraining when using FSDP NO_SHARD strategies as compared to PyTorch’s Distributed Data Parallel (DDP). We leveraged this knowledge for pretrained each of our OREOLE-MR models using the FSDP NO_SHARD strategy to distribute an effective batch size of 2048 across 4 NVIDIA A100 (80GB) GPUs composing NVIDIA DGX clusters.

Table 7: Implementation details adopted for pretraining of OREOLE-MR and OREOLE-HR model variants.

Details	OREOLE-MR	OREOLE-HR
Optimizer	AdamW	AdamW
	$\beta = (0.9, 0.95)$	$\beta = (0.9, 0.999)$
LR ¹	1.2e-3	2.4e-3
LR scheduler	CosineAnnealingLR	CosineAnnealingLR
Effective BS	2048	4096
Warmup	40 epochs	40 epochs
Image size	224x224	512x512
Image bands	RGB	BGR+NIR
Weight Decay	0.05	0.05
Augmentation	RandomResizedCrop	RandomResizedCrop
	(crop ratio 0.2-1.0)	(crop ratio 0.2-1.0)
	RandomHorizontalFlip	RandomHorizontalFlip

¹ *base_lr* is set to $1.5e-4$ and scaled as $lr = base_lr \times 4096/256$ following [24];

7.2 Image classification experiments details

Datasets *UC Merced (UCM)* is a image classification dataset containing 2100 remote sensing images from the USGS National Map, at a resolution of 1ft. Images are $256 \times 256px$ large, distributed evenly across 21 categories. The *AID* dataset was compiled from multisensor data available in Google Earth, with spatial resolutions $0.5 - 8m/px$ for images $600 \times 600px$ large. It contains 10k images distributed across 30 categories, with class distributions ranging from 220 to 400 images each. Finally, the *NWPU-RESISC45* dataset contains 31.5k images evenly distributed across 45 categories and also collected from Google Earth for regions distributed across the world. Image are $256 \times 256px$ large, with spatial resolutions ranging from 0.2 to $30m/px$. We adopt the following splits for each dataset: *UCM* ($TR = 50\%$) with 1050/1050 train/test images; *AID* ($TR = 20\%$) with 2000/8000 images; *NWPU* ($TR = 10\%$) with 3150/28350 images.

Implementation details The MLP heads of pretrained models are replaced by a linear classifier for supervised training while keeping the weights for the rest of the model frozen. The setup in [47] reports experiments for 200 epochs of tuning with batch-size 256 for all three datasets while adapting usage of the LARS optimizer[56] with a base learning rate of 0.1 and no weight decay. As discussed in Section 4, we empirically observe that while keeping the same batch size, increasing the base learning up to 10 in this setup yields severe improvements in accuracy levels reached after linear probing. Thus, for linear probing evaluation with QUETZAL-MR model variants we adopt LARS with base learning rate 10, tuning the learnable heads for 100 epochs with a warmup period of 10 epochs.

7.3 Object detection experiments details

Datasets DIOR [30] contains 23,463 $800 \times 800px$ RGB images sourced from Google Earth, with $GSD = 0.5 - 30m/px$. There are 20 object classes and a total of 192,472 object instances. DIOR is divided into training, validation, and testing sets with 5,862, 5,863, and 11,738 images, respectively. As in [46], we use the training and validation sets in a combined 11,725-image "trainval" set for fine-tuning, and we validate using the testing set. The images, object classes, object instances, and data splits are identical to DIOR.

Implementation details We augment our pretrained ViT backbones weights into VitDet [31], a ViT-based object detection architecture that demonstrates promising performance with minimal adaptation of backbones required. Faster-RCNN [22] was used as the detection head for the horizontal object detection task, and its variant Oriented Faster-RCNN was used for the oriented object detection task. The VitDet implementation was based on *mmdetection* [9] for DIOR data, and the same implementation was further adapted for DIOR-R data using the *mmrotate* [59] library. We report evaluation based on Mean Average Precision (mAP) calculated at Intersection over Union (IoU) threshold 50%.

As in [31], we adopt a patch size of $16 \times 16px$ for all ViT backbones, interpolating the originally $14 \times 14px$ patch embeddings pretrained for the ViT-H and ViT-1B backbones. With the pretrained ViT weights, we finetuned on DIOR and DIOR-R for 12 epochs, the same as the setting in [46]. Similar to [47], the base learning rate was set as $1e - 4$ for ViT-B with a batch size of 4. Experimentation with $[1, 3, 5, 10]e - 4$ and same batch size for ViT-G has shown better convergence with $3e - 4$, while for ViT-B the original $1e - 4$ revealed to be better. The remaining configurations follow [46] and are listed in the Table 8. Convergence issues are faced with ViT-H and ViT-e(3B) configurations, as curves in Figure 2a show. As discussed in Section 4, we conjecture the complexity of the object detection head and the need for different learning decay policies for different model sizes [31] are potential root causes.

Table 8: Summary of hyperparameters and additional configuration details adopted for linear probing and finetuning experiments.

	Image classification			Object detection	Semantic segmentation	
Details	UCM	AID	NWPU	DIOR-R	Potsdam	LoveDA
Head/decoder	Linear Probing	Linear Probing	Linear Probing	Faster/Oriented Faster RCNN	UperNet+FCN	UperNet+FCN
Optimizer	LARS	LARS	LARS	AdamW	AdamW	AdamW
Input size	256	600	256	800	512	1024
Training samples	1,050	2,000	3,150	11,725	3,456	4,191
Test samples	1,050	8,000	28,350	11,738	2,016	1,796
Effective batch size	256	256	256	4	256	256
Base LR	10	10	10	ViT-B: $1e-4$ ViT-H,1B,3B: $3e-4$	$5e-4$	$5e-4$
Warmup	10 epochs	10 epochs	10 epochs	500 iter	50 epochs	50 epochs
LR scheduler	CosineAnnealingLR			StepLR: $\gamma = 0.1$, decay at epochs [8, 11]	CosineAnnealingLR	CosineAnnealingLR
Weight Decay	0	0	0	0.05	0.05	0.05
Duration	100 epochs	100 epochs	100 epochs	12 epochs	100 epochs	100 epochs
LR layer wise decay rate	0.9	0.9	0.9	0.9	0.9	0.9
Drop path rate	-	-	-	0.1	0.	0
Augmentation	RandomResizedCrop (224) RandomHorizontalFlip			RandomFlip	RandomResize (0.5-2.0) RandomCrop RandomFlip PhotoMetricDistortion	
Loss function	CE	CE	CE	CE	CE FCN weight: 0.4	

7.4 Semantic segmentation experiments details

Datasets. The LoveDA [48] comprises of 5987 high resolution imagery ($1024 \times 1024px$, $GSD = 0.3m/px$) from Google Earth, with per-pixel annotations of 7 land cover classes. Images are split into train/val/test sets comprising 2522/1669/1796 samples respectively. The evaluation metrics have been computed on the test set using the evaluation server. The ISPRS Potsdam dataset consists of 38 tiles of $GSD = 0.5m/px$

orthoimagery, annotated with 6 land cover classes. Like related works, we tile images into $512 \times 512px$ patches, with train/test sets comprising of 3456/2016 patches.

Implementation details. Following common practice across related works [23, 40, 45], we adopt the UperNet scheme [51] to compose segmentation frameworks for all our considered pretrained backbones. All experiments are implemented using the *mmsegmentation* codebase. Following [45, 47], we configured the UperNet architectures with a Feature2Pyramid neck operating with $[4, 2, 1, 0.5]$ rescaling factors. For ViT-B configurations, features are collected from blocks [3, 5, 7, 11] (index starting at 0) of the 12-layer deep backbone. Since the ViT-H and ViT-g(1B) variants are 32-layers deep, we instead collect features from blocks [11, 17, 23, 31]. Moreover, a FCN with 256 channels and loss weight of 0.4 is used as auxiliary head. While we adopt such architectural configuration for consistency with the literature, experiments with the ViT-e(3B) remain as future work since its pairing UperNet + auxiliary FCN head does not fit in a single GPU for our setups, requiring further development using model sharding.

Configurations reported in [47] and [8] employ 160k iterations at batch size 8, base LR of $6e-5$ and weight decay of 0.01 for Potsdam and LoveDA, while [40] and [23] adopt 80k iterations for the same set of hyperparameters on Potsdam. This corresponds to finetuning durations of 1.28M and 0.64M iterations at batch-size 1. To efficiently evaluate different model sizes across several configurations, we conduct these experiments under a distributed computing setup where such a small batch size is sub-optimal. Following experimentation with base learning rates for ViT-B on Potsdam, for all our semantic segmentation experiments we adopt an effective batch-size of 256, with a base learning rate of $5e-4$ paired with CosineAnnealingLR scheduled with 50 epochs of warmup and finetuning duration of 100 epochs for each dataset. This corresponds to 345.6k iterations (at batch size 1) for Potsdam and 419.1k iterations for LoveDA, which is equivalent to only 27% of the iterations reported by [8, 47] for Potsdam and 65.5% of the duration reported in [47] for LoveDA.

7.5 OREOLE-HR experiments details

Similar to experiments reported in section 7.4, UperNet is paired to pretrained OREOLE-HR variants for semantic segmentation. Feature pyramids and rescaling factors are the same as reported in section 4, with the auxiliary FCN head however removed to reduce computing workload. We adopt distance-labels as per [53] to formulate the loss function, and experiments are performed with a effective batch size of 2048, AdamW with betas (0.9, 0.999), base learning rate of $1e-3$, and a cosine annealing LR schedule with 10 epochs of warmup. Image size of 512×512 is adopted for ViT-B configurations and 504×504 for larger configurations trained with patches $14 \times 14px$ large, to bypass mmsegmentation errors related to non-integer number of patches.

7.6 OREOLE-MR - additional results

Figure 2c additionally summarizes performances of our models when using 1, 10, and 50% of the total available training data for DIOR-R (object detection) and Potsdam (semantic segmentation) datasets. Here we highlight a lack of reproducibility details on related works, which report maintaining the same FT configuration when performing experiments with different data percentages. Such description is insufficient when training duration and schedules are reported in terms of number of epochs instead of iterations. For our experiments, we opted for maintaining the same number of training iterations for training data budgets considered, since the goal is to assess the sample efficiency of the models, not their sensitivity to training duration (iterations). Our results show consistent benefits of a larger model when $> 10\%$ (1170) training images of DIOR-R are used, and as low as 1% (35) training images for Potsdam. For DIOR-R, ViT-B values at lower sample budgets are significantly higher than the ones reported by [8], which we conjecture is due to our configuration maintaining the same number of iterations as when finetuning with full dataset.

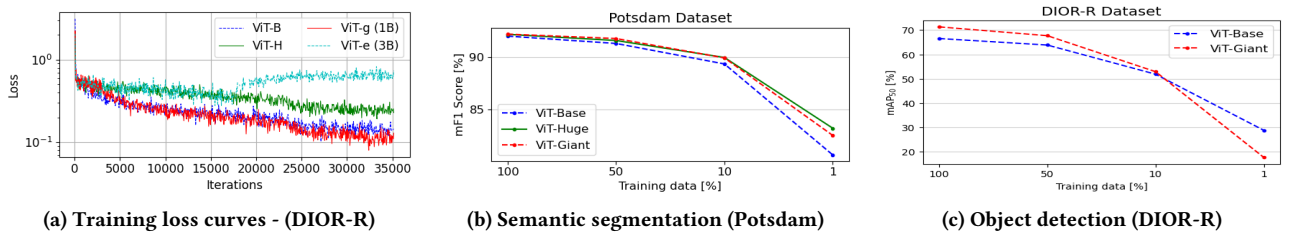


Figure 2: Convergence curves for object detection configurations, and finetuning results for object detection and semantic segmentation experiments with varying training set sizes.

Qualitative examples Figure 3 provides qualitative examples comparing outputs provided by ViT-B(top) and ViT-G(1B) (bottom) model variants for composing the test set of the DIOR-R dataset. Noticeable improvements are the detections of airplanes by ViT-g(1B) in the first image, and removal of false positives in the second example from the left.

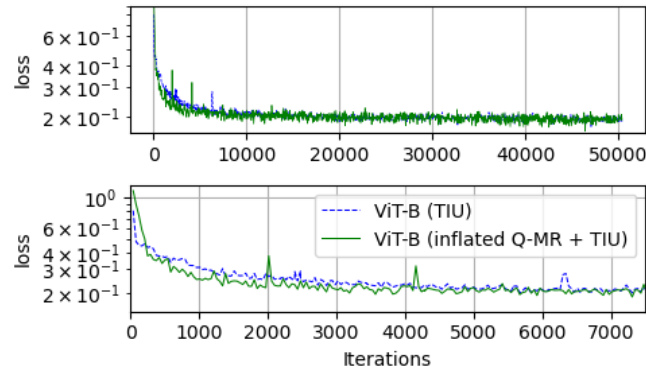
Table 9: Results for finetuning OREOLE-MR with frozen backbone (Frozen/Not-Frozen)

Method	Backbone	Potsdam [mF1%]	DIOR-R [mAP%]
OREOLE-MR	ViT-B	88.97/92.01	68.33/68.58
OREOLE-MR	ViT-H	89.75/92.18	/
OREOLE-MR	ViT-G (1B)	89.62/92.20	71.06/71.31

**Figure 3: Examples of detections provided by our OREOLE-MR ViT-B(top) and ViT-G(1B) (bottom) model variants for composing the test set of the DIOR-R dataset.**

7.7 OREOLE-HR additional results

Initialization using inflated OREole-MR pretrained weights In addition to improved $F1$ results discussed in Section 5, the loss curves in 4 show how initialization with pretrained OREOLE-MR weights inflated with a 4th band yield faster convergence (i.e., better starting point) for MAE pretraining on our 4-band datasets.

**Figure 4: Loss curves for OREOLE-HR models pretrained from scratch vs with OREOLE-MR pretrained weights inflated with an extra randomly initialized 4th band.**

Qualitative results Figure 5 provides a qualitative example comparing BFE outputs by a ViT-H pretrained in TIU (in blue) compared to a ViT-B pretrained on ORB only (in pink). ViT-H outputs improve adherence to building boundaries in both examples, and retrieving better delineations including in areas of low image contrast (e.g., lower-left building in left-most example).



Figure 5: Qualitative example comparing BFE outputs by a ViT-H pretrained in TIU (in blue) compared to a ViT-B pretrained on ORB only (in pink).